Warm-Sector Heavy Rainfall in Southern China and Its WRF Simulation Evaluation: A Low-Level-Jet Perspective

MURONG ZHANG AND ZHIYONG MENG

Laboratory for Climate and Ocean–Atmosphere Studies, Department of Atmospheric and Oceanic Sciences, School of Physics, Peking University, Beijing, China

ABSTRACT

Warm-sector heavy rainfall in southern China refers to the heavy rainfall that occurs within the warm sector hundreds of kilometers south of a front or without a front during April–June, characterized by poor predictability and a close relationship with low-level jets (LLJs). Based on 45 warm-sector heavy rainfall episodes in 2013 and 2014 in southern China, this study examines their general characteristics and evaluates the performance of convection-permitting WRF Model simulations from an LLJ perspective. The results show that 64% of the warm-sector heavy rainfall episodes are associated with an LLJ (LLJ type) and 36% are not (no-LLJ type). The LLJ type is distinct from the no-LLJ type, with large rainfall accumulation along the coastal area. It is more common for LLJs to occur at both 800 and 925 hPa in the LLJ type, where there is a wide 800-hPa LLJ west of Guangdong Province and two 925-hPa LLJs over Beibu Gulf and the South China Sea (SCS). The coastal convergence associated with the terminus of the LLJ on 925 hPa is conducive to the coastal rainfall. WRF generally presents lower QPF skill in the LLJ type than in the no-LLJ type, due to the severe underestimation of coastal rainfall. The QPF skill of the LLJ type is significantly correlated with the forecast accuracy of LLJs, especially at 925 hPa. The north bias of the simulated LLJ on 925 hPa over the SCS and the associated overestimation of wind speed below ~900 hPa over the inland region weaken the coastal convergence and eventually lead to the underestimation in coastal precipitation.

1. Introduction

The presummer rainy season (April–June) is the first rainy season in southern China. It occurs during the early stage of the East Asian summer monsoon (Ding 1994) and contributes approximately half of the annual precipitation amount in southern China (Luo et al. 2017). During the presummer rainy season, the heavy rainfall associated with mesoscale convective systems (MCSs) frequently takes place in southern China in the warm sector hundreds of kilometers to the south of a cold or quasi-stationary front or without any front (e.g., Luo et al. 2013; Wang et al. 2014; Wu and Luo 2016), which is often termed warm-sector heavy rainfall (Huang 1986). Without strong synoptic-scale forcing, the precipitation in the warm sector is greatly influenced by monsoonal inflow from the South China Sea (SCS) (e.g., Chen et al. 2017; Zhang and Meng 2018) and modulated by the land–sea contrast (Chen et al. 2015; Chen et al. 2016) and complicated terrain

(Chen et al. 2018) (Fig. 1) in southern China. With these unique and complex multiscale atmospheric processes, the warm-sector heavy rainfall often occurs abruptly without perceptible prediction clues and produces local extreme precipitation with relatively poor quantitative precipitation forecast (QPF) skill (He et al. 2016), leading to severe floods and considerable losses of life and property (Zhou et al. 2003).

The low-level jet (LLJ) is commonly observed in southern China during presummer rainy season (e.g., Du et al. 2014; Luo et al. 2017). The LLJs over this region can be generally classified into two types (Chen et al. 1994; Du et al. 2012, 2014). The first type is synoptic-system-related LLJ (SLLJ), which occurs within low-level free troposphere (900–600 hPa); the second type is boundary layer jet (BLJ), which occurs in the boundary layer and can be influenced by both boundary processes and large-scale weather systems (Du and Chen 2018). Inertial oscillation, land–sea thermal contrast, orographic blocking, or ageostrophic winds offshore veering southward by the Coriolis force and combining with the southerly

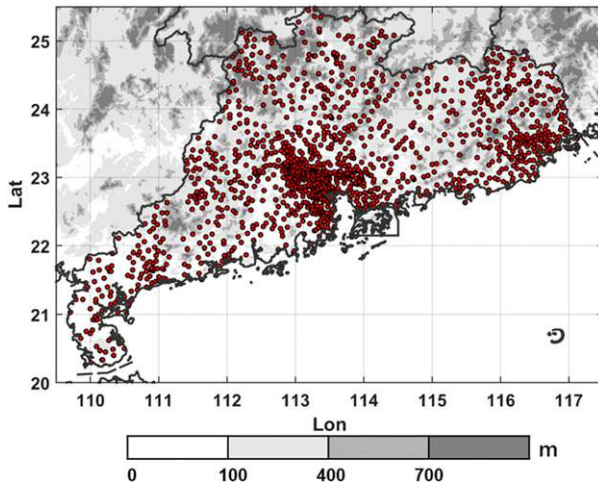*Corresponding author*: Zhiyong Meng, zymeng@pku.edu.cn

FIG. 1. Topography (shaded) of the region of focus over southern China and the rain gauge distribution (red dots) in Guangdong Province.

geostrophic wind have been considered as important formation mechanisms for southerly BLJs in this region (Du et al. 2014, 2015). The formation of southwesterly SLLJs in this region is usually associated with low-level baroclinicity relevant to extratropical cyclone to the north of southern China (Du et al. 2014),

southwest vortex (Zhang and Meng 2018), or diabatic effects (Chen and Yu 1988; Chen 1982).

LLJs advect warm and moist air from SCS and Beibu Gulf to southern China and serve as prominent source of instability for heavy-rain-producing MCSs. Based on ensemble sensitivity analyses of a presummer extreme rainfall event in 2014 in southern China, Zhang and Meng (2018) found that rainfall intensity was highly sensitive to the upstream low-level moisture flux. In addition, the LLJ provides dynamical forcing that enhances the vertical motion favorable for the initiation and maintenance of heavy rainfall events (Zhang et al. 2016; Du and Chen 2018). Based on a case study, Du and Chen (2018) proposed that convergence near the terminus of the BLJ overlapped with the divergence near the entrance of the SLLJ was quite important for the initiation of the warm-sector heavy rainfall in coastal region in southern China. LLJ may also contribute to elevated convection initiation in warm sector through enhancing adiabatic cooling by weak vertical ascent and sufficient horizontal moisture transport (Zhang et al. 2019). However, most previous studies on LLJs in warm-sector heavy rainfall have focused on the mechanisms of individual cases. A good understanding of the general characteristics of warm-sector heavy rainfall and associated LLJs and the relationship between them is of
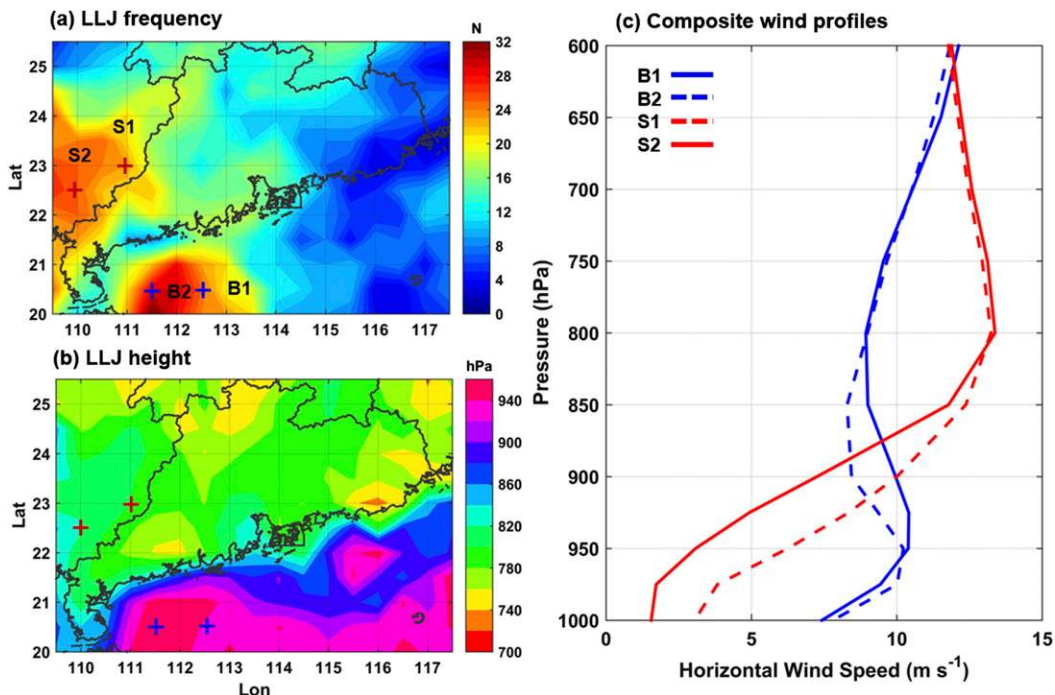

FIG. 2. (a) Distribution of the frequency of LLJ occurrence within the 29 LLJ-type warm-sector heavy rainfall episodes (including start and end times). (b) Distribution of average LLJ heights of LLJ-type episodes (including start and end times). (c) Composite horizontal wind speed profiles of LLJ-type episodes at B1, B2, S1, and S2 [locations denoted in (a),(b)].
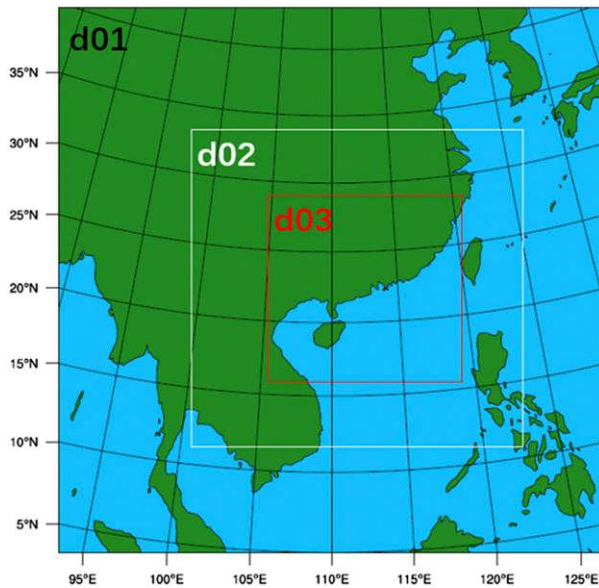
FIG. 3. WRF nested domains for the verification experiments.

TABLE 1. Statistics of warm-sector heavy rainfall episodes.

Year	LLJ	no-LLJ	Total
2013	16	7	23
2014	13	9	22
Total	29 (64%), including 21 DLLJ, 6 SLLJ, and 2 BLJ.	16 (36%)	45

southern China and its relationship with QPF skill are yet to be revealed. Understanding the limitations of LLJ forecasts in warm-sector heavy rainfall and how influential the LLJ is on precipitation forecasts is of vital importance to eventually improve the QPF skills.

Based on 45 warm-sector heavy rainfall episodes collected from the presummer rainy season in Guangdong Province (Fig. 1) in southern China in 2013 and 2014, the present study is aimed at demonstrating the general characteristics of warm-sector heavy rainfall in southern China and the associated QPF skill in convection-permitting WRF Model simulations from an LLJ perspective. Specifically, statistics, diurnal variations and the rainfall distribution of different types of warm-sector heavy rainfall in terms of LLJs were obtained; typical LLJ structures and their association with heavy rainfall were revealed through composite analyses. In addition, the QPF skill of convection-permitting WRF Model simulations for warm-sector heavy rainfall was evaluated for the identified heavy rainfall episodes; the model deficiencies in predicting precipitation and LLJs and the relationship between the accuracy of simulated LLJs and QPF skill were investigated. Section 2 describes the data and methods used in this study. Section 3 presents the general characteristics of warm-sector heavy rainfall and LLJs. The QPF skill of warm-sector heavy rainfall and the LLJ forecast accuracy and their relationship are also evaluated in section 3. Section 4 summarizes the study's key findings.

great practical use in daily forecasting but is still lacking in the literature. Moreover, how the relationship between LLJ and warm-sector heavy rainfall differs from the well-established relationships between LLJ and convective precipitation elsewhere in the world (e.g., Stensrud 1996) is also worth investigating to expand current knowledge.

To improve the prediction of warm-sector heavy rainfall, it is necessary to evaluate the QPF skill and understand the model deficiencies in predicting the precipitation and associated physical processes. Huang and Luo (2017) provided a concise evaluation of the QPF performance of five mainstream global ensemble prediction systems for southern China during the presummer rainy season. They found that locally produced torrential rainfall is less predictable than the rainfall associated with synoptic-scale forcing in global models, even with shorter forecast lead times. Nevertheless, the performance of regional convection-permitting WRF Model simulations in warm-sector heavy rainfall remains unknown. Zhang et al. (2016) demonstrated the positive impact on QPF of assimilating wind profiling radar observations in the Global/Regional Assimilation and Prediction System during the presummer rainy season in southern China, implying the importance of accurate low-level wind observations in QPF over this region. Squitieri and Gallus (2016) examined the forecast accuracy of LLJs over the Great Plains in the United States and proved the significant correlations between total wind direction and MCS precipitation forecast skill. However, the general forecast accuracy of LLJs in warm-sector heavy rainfall in

2. Data and methods

a. Observational and analysis data

The hourly rainfall observations used in this study were from a dense network of automated rain gauges over Guangdong Province (Fig. 1) operated by Guangdong Meteorological Bureau, totaling 1394 in 2013 and 2014. The rain gauges were generally distributed evenly, except over river deltas, where the terrain is flat and the gauges are denser. The hourly rainfall observations were interpolated into a $0.1° \times 0.1°$ grid for the convenience of comparison with simulated
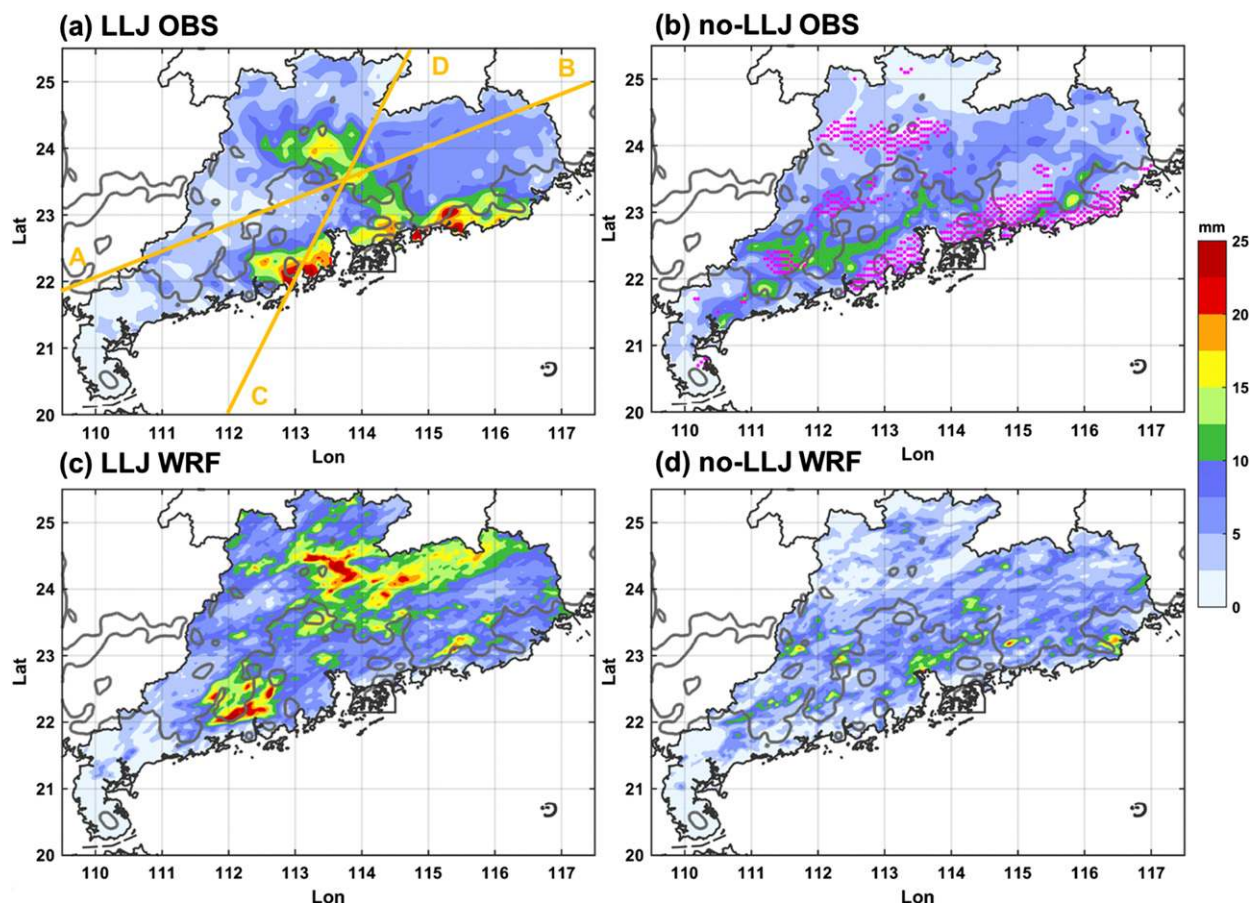
FIG. 4. Composite 6-h-accumulated precipitation (shaded) of observations for (a) LLJ-type and (b) no-LLJ-type warm-sector heavy rainfall episodes. (c),(d) As in (a),(b), but for WRF simulations. The terrain height of 100 m is contoured in bold gray. The magenta dots in (b) denote where the difference between the composite observation of LLJ and no-LLJ types are significant at 90% level by Welch's *t* test. The yellow lines in (a), which are also given in Fig. 6, denote the paths along which the vertical cross sections in Fig. 7 are plotted.

rainfall. Synoptic charts obtained from the China Meteorological Administration (CMA) provide the synoptic conditions for the identification of warm-sector heavy rainfall. The National Centers for Environmental Prediction Global Forecast System (GFS) analysis (Kalnay et al. 1990; Kleist et al. 2009), with a horizontal grid spacing of 0.5° and a 6-h time interval, was used for composite analyses and the identification of LLJs. GFS analysis was also used as the initial and boundary conditions in the WRF simulations.

b. Criteria for identifying warm-sector heavy rainfall episodes and LLJs

During the presummer rainy season (April–June) in 2013 and 2014, warm-sector heavy rainfall episodes were identified based on the following criteria:

1) The gauge-observed rainfall accumulation is greater than 50 mm in a 6-h time range (0000–0600, 0600–1200, 1200–1800, and 1800–0000 UTC)

in a contiguous area extending at least 50 km in at least one direction in Guangdong Province considering that the MCSs and their associated rainfall areas in warm sector could be in various shapes.

2) The geometric center of heavy rainfall is at least 200 km away from the synoptic front at any pressure level during the heavy rainfall episode (Ding et al. 2011; He et al. 2016). The information of synoptic fronts and the northern cold highs used in the following criteria (number 3) were obtained from CMA operational analysis synoptic charts.

3) The synoptic conditions with northern cold high near the surface intruding into Guangdong Province were excluded to avoid the influence of cold air from the north following He et al. (2016). In addition, the heavy rainfall is not associated with tropical cyclones.

Following Du et al. (2014), the LLJ was identified as when the maximum wind speed is greater than 10 m s^{-1}

under 600 hPa and the wind speed decreases by at least $3 \, \text{m s}^{-1}$ from the height of the wind maximum to the wind minimum above that. In addition, the low-level jets identified in the current study are characterized by southerly wind components given the typical synoptic-scale patterns of warm-sector heavy rainfall in southern China. For a warm-sector heavy rainfall episode, if there are grid points that satisfy the LLJ definition in the range of 200 km from the rainfall center at either the start or the end time of the 6-h rainfall episode and these grid points are contiguously extending for at least 100 km in at least one direction, then the episode is classified as the LLJ type.

Based on the 29 LLJ-type episodes obtained using the LLJ criteria in the present study, we examined the distribution of the frequency and the average LLJ height (Figs. 2a,b). Two high-frequency areas of LLJ occurrence are located to the west and south of Guangdong Province (Fig. 2a) with the jet heights at ~840–780 and ~900–960 hPa, respectively (Fig. 2b). Following the definition of SLLJ and BLJ in Du et al. (2012) and Du et al. (2014), in the current study, the LLJ with jet height no higher than 900 hPa is classified as BLJ and the LLJ with jet height higher than 900 hPa as SLLJ. Therefore, these two high-frequency areas correspond to SLLJ and BLJ, respectively. The vertical wind profiles in these two areas (Fig. 2c) reveal distinct features of these two types of LLJs: the SLLJ (e.g., S1 and S2) to the west of Guangdong has higher jet height with larger jet intensity, while the BLJ (e.g., B1 and B2) to the south of Guangdong has lower jet height with smaller jet intensity. Given that the mean jet heights of SLLJ and BLJ (over the domain of Fig. 2a) are 800.4 and 932.8 hPa, the horizontal wind speed at 800 and 925 hPa were chosen to represent the characteristics of SLLJ and BLJ. Considering that the horizontal jet stream over certain threshold of total wind speed is frequently used as the guidance in operational forecasts over southern China (Huang 1986; Ding et al. 2011), for those LLJ type episodes in the present study, if there are grid points with the horizontal wind speed at 800 hPa (925 hPa) larger than $10 \, \text{m s}^{-1}$ in the range of 200 km from the rainfall center at either the start or the end time of the 6-h rainfall episode and these grid points are contiguously extending for at least 100 km in at least one direction, then the episode is classified as the SLLJ (BLJ) type. Heavy rainfall episodes associated with both the SLLJ and BLJ are classified as the double-LLJ (DLLJ) type.

c. Numerical model configurations

The identified warm-sector heavy rainfall episodes were simulated using version 3.9.1.1 of the WRF-ARW Model (Skamarock et al. 2008). Initial and lateral
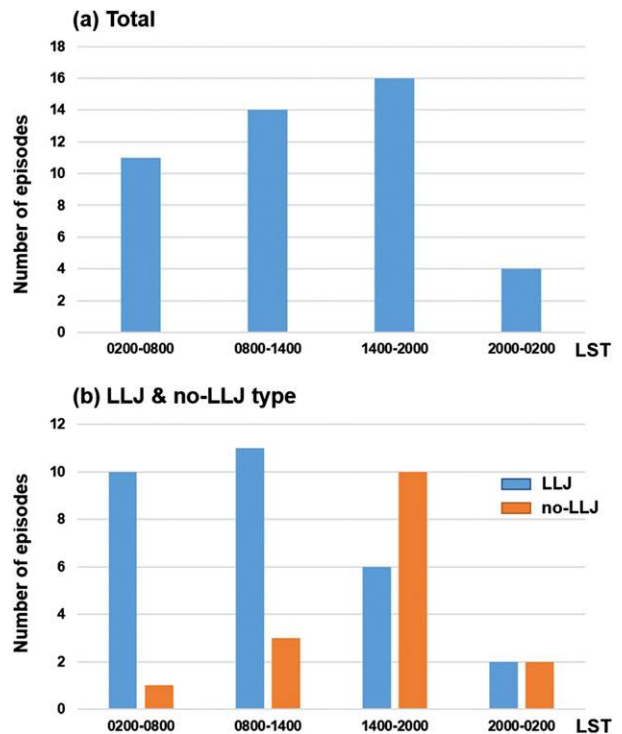

FIG. 5. Diurnal variation of the frequency of (a) all and (b) LLJ- and no-LLJ-type warm-sector heavy rainfall episodes.

boundary conditions were obtained from GFS analysis (gridded at $0.5° \times 0.5°$), and the lateral boundary conditions were updated every 6 h. Three two-way nested domains (Fig. 3) with 40 stretched vertical levels (following Du et al. 2014) and 27-, 9-, and 3-km horizontal grid spacings were used. All simulations were initialized 12 h before the episode of interest started, and integrated for 36 h with a spin-up period over 0–12 h, since previous studies have indicated that the model performs best at short ranges over 12–36 h (e.g., Chien and Jou 2004; Wang et al. 2017). The WRF single-moment 5-class microphysics scheme (WSM5; Hong et al. 2004), the Yonsei State University PBL scheme (YSU; Hong et al. 2006), the Dudhia shortwave (Dudhia 1989), and the Rapid Radiative Transfer Model (RRTM) longwave radiation scheme (Mlawer et al. 1997) were used for all three domains. The Grell–Devenyi ensemble cumulus scheme (Grell and Devenyi 2002) was used for d01 and d02. No cumulus parameterization was used for d03.

d. Objective evaluation metrics

The equitable threat score (ETS) and the bias score (BS) (Wilks 1995; Jolliffe and Stephenson 2003; Wang et al. 2017) are widely used in the evaluation of QPF skill. At a given rainfall threshold, they are defined as
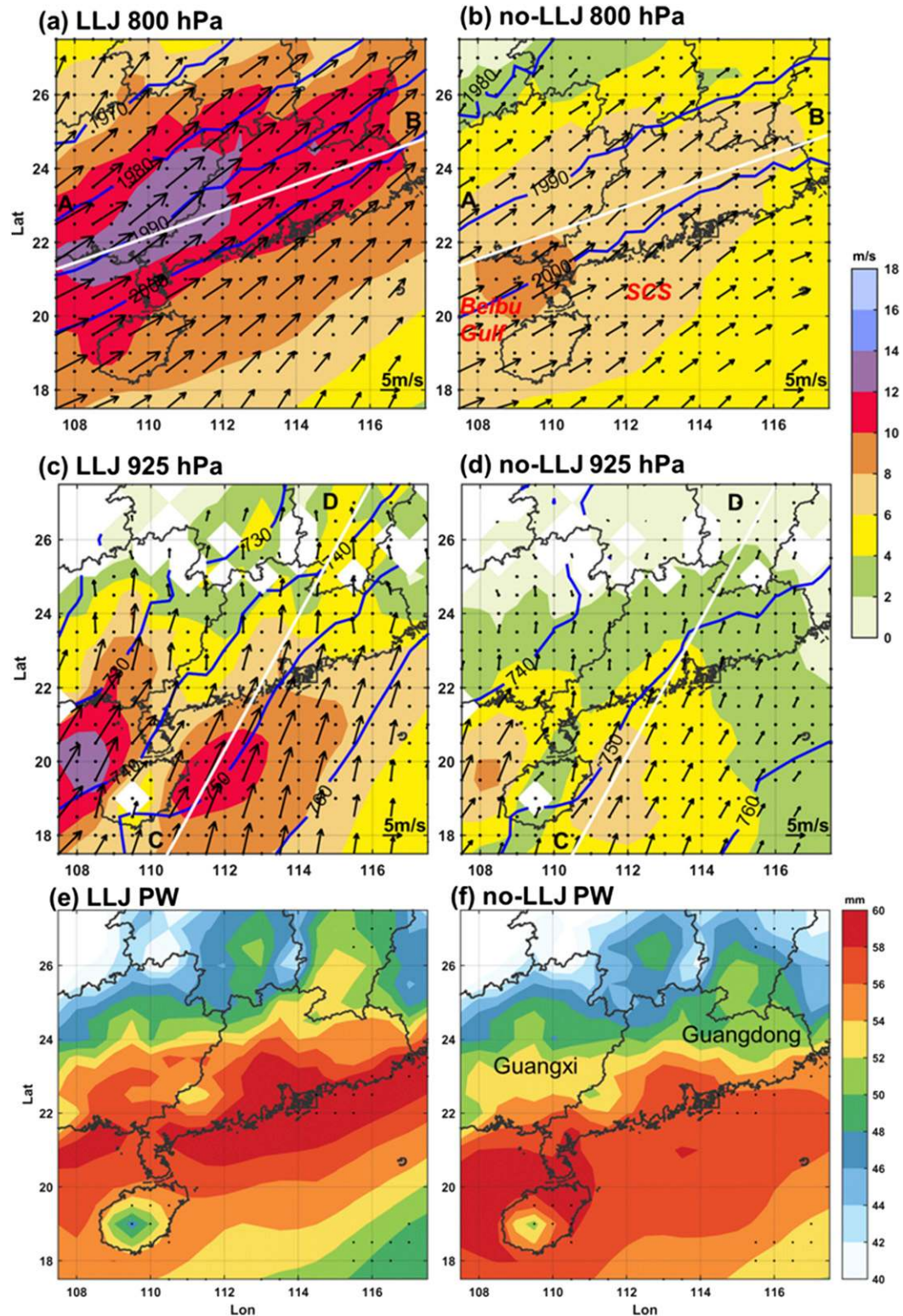
FIG. 6. Composite low-level synoptic environment at the start time of different types of warm-sector heavy rainfall episodes revealed by GFS analysis, including geopotential height (contoured in blue every 10 gpm), horizontal wind speed (shaded every $2 \, \mathrm{m \, s^{-1}}$), and wind vector at (a) 800 hPa in the LLJ type, (b) 800 hPa in the no-LLJ type, (c) 925 hPa in the LLJ type, and (d) 925 hPa in the no-LLJ type, and precipitable water (shaded every 2 mm) of (e) the LLJ type and (f) no-LLJ type. The paths for the vertical cross sections in Fig. 7 are given in
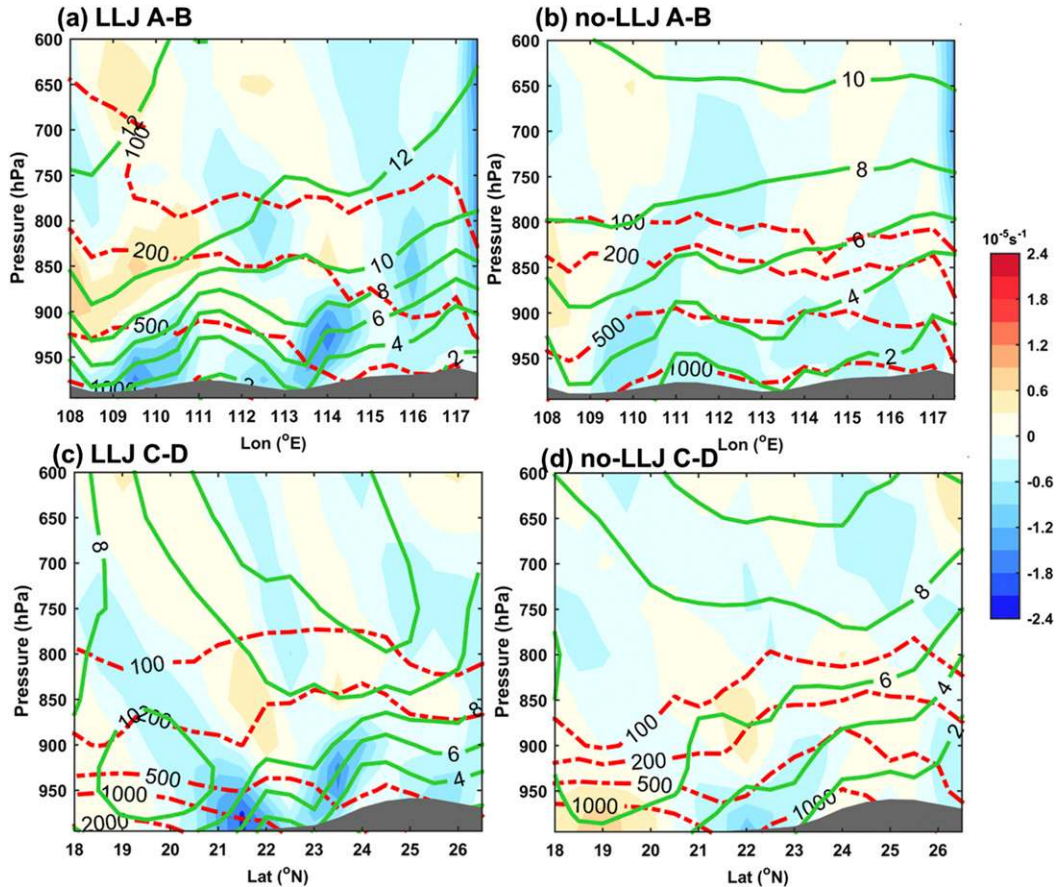
FIG. 7. Composite vertical cross sections at the start time of (a) LLJ-type (path A–B in Fig. 6a) and (b) no-LLJ-type (path A–B in Fig. 6b) warm-sector heavy rainfall episodes revealed by GFS analysis, including horizontal divergence (shaded every $0.3 \times 10^{-5}\,\mathrm{s}^{-1}$), horizontal wind speed (contoured every $2\,\mathrm{m\,s}^{-1}$ in bold green), and CAPE (contoured at 100, 200, 500, 1000, and 2000 J kg^{-1} in dashed red). (c),(d) As in (a),(b), but for the vertical cross sections along path C–D given in Figs. 6c and 6d.

$$ETS = (H - R)/(H + M + FA - R), \qquad (1)$$

$$R = (H + M) \times (H + FA)/N, \qquad (2)$$

$$BS = (H + FA)/(H + M), \qquad (3)$$

where H, M, and FA are the number of hits (observed and predicted), misses (observed but not predicted), and false alarms (predicted but not observed), respectively, among all verification points N. The ETS is the fraction of correctly predicted observed events excluding random hits. A perfect ETS is 1.0, while $-1/3$ is the lower limit and 0 is the threshold for no skill. The BS is the ratio between predicted and observed events, with 1 as the threshold for over (>1) and under (<1) prediction.

In the present study, the ETS and BS were also calculated through a neighborhood-based method following Clark et al. (2010, hereafter C10), who used circular geometry with radius r to define neighborhoods. Quoting C10 (p. 1499): "If an event is observed at a grid point, this grid point is a hit if the event is forecast at the grid point or at any grid point within a circular radius r of this observed event. Similarly, if an event is forecast at a

←

(a)–(d) (bold white lines, same as the yellow paths given in Fig. 4a). The referenced vector is given in the bottom right. Beibu Gulf and the South China Sea (SCS) are denoted in (b). The black dots in (a)–(d) denote where the difference between the composite horizontal wind speed of LLJ and no-LLJ types are significant at 90% level by two-tailed Welch's t test. The black dots in (e),(f) denote where the difference between the composite precipitable water of LLJ and no-LLJ types are significant at 90% level by two-tailed Welch's t test. The locations of Guangdong and Guangxi Provinces are given in (f).
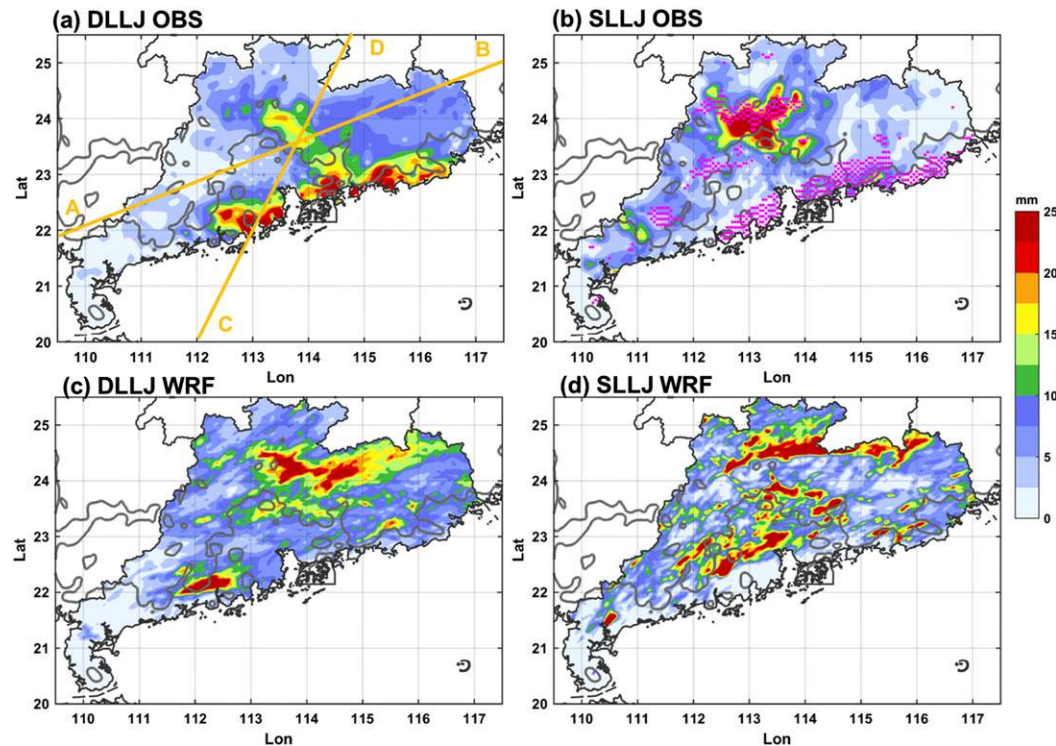
FIG. 8. Composite 6-h-accumulated precipitation (shaded) of observations for (a) DLLJ-type and (b) SLLJ-type warm-sector heavy rainfall episodes. (c),(d) As in (a),(b), but for WRF simulations. The terrain height of 100 m was contoured in bold gray. The magenta dots in (b) denote where the difference between the composite observation of DLLJ and SLLJ types are significant at 90% level by Welch's *t* test. The yellow lines in (a), which are also given in Fig. 9, denote the paths along which the vertical cross sections in Fig. 11 are plotted.

grid point, the grid point is a hit if an event is observed at the grid point or at any grid point within *r* of this forecast event. A miss is assigned when an event is observed at a grid point and none of the grid points within *r* forecast the event, and false alarms are assigned when an event is forecast at a grid point and not observed within *r* of the forecast. Correct negatives are assigned in the same way as for the traditional ETS computation.'' Unlike the traditional point-to-point criteria, the neighborhood-based criteria are relaxed by considering the adjacent grid points within a specified radius of influence, which avoids the punishment of small displacement errors in decent forecasts (Ebert 2008; Squitieri and Gallus 2016). Compared with other neighborhood-based definitions such as McMillen and Steenburgh (2015) and ''neighborhood maximum'' approach (e.g., Sobash et al. 2011; Barthold et al. 2015), C10's criteria produce less misses and false alarms but more correct negatives, leading to higher ETSs, thus C10 method is more lenient (Schwartz 2017). Considering the rather limited predictability of warm-sector heavy rainfall in southern China, it may be more appropriate to examine the QPF skills using C10's criteria. Both rain gauge observations and WRF simulations were interpolated into a 0.1° × 0.1° grid for the

evaluation. The 6-h accumulated rainfall of each rainfall episode on the grid points over Guangdong Province (Fig. 1) was evaluated with a radius of influence of 0.5° [$ETS_{r=5}$, hereafter, *r* represents the number of grid spacing for analysis (0.1°)] and without a radius of influence ($ETS_{r=0}$).

To evaluate the LLJ as object and avoid the subjectivity in identifying LLJ position and strength in each episode, we applied the ETS and BS approach (without a radius of influence) for total wind speed at 800 and 925 hPa similar to precipitation but looking at grid points where the total winds meet certain thresholds. Given a certain threshold of total wind speed that can be used to identify LLJs, ETSs and BSs can be used to evaluate the forecast accuracy of LLJ distribution and strength to some extent. Following Squitieri and Gallus (2016), for each 2D wind field at the start time of the rainfall episode, the threshold was chosen as the 65th percentile of the total wind speed at certain pressure levels over the domain bounded by 17.5°–27.5°N and 107.5°–117.5°E, which means only the top 35% strongest wind speeds were considered. In addition, the forecast accuracy of LLJs and associated weather variables was also measured by mean error (ME) over
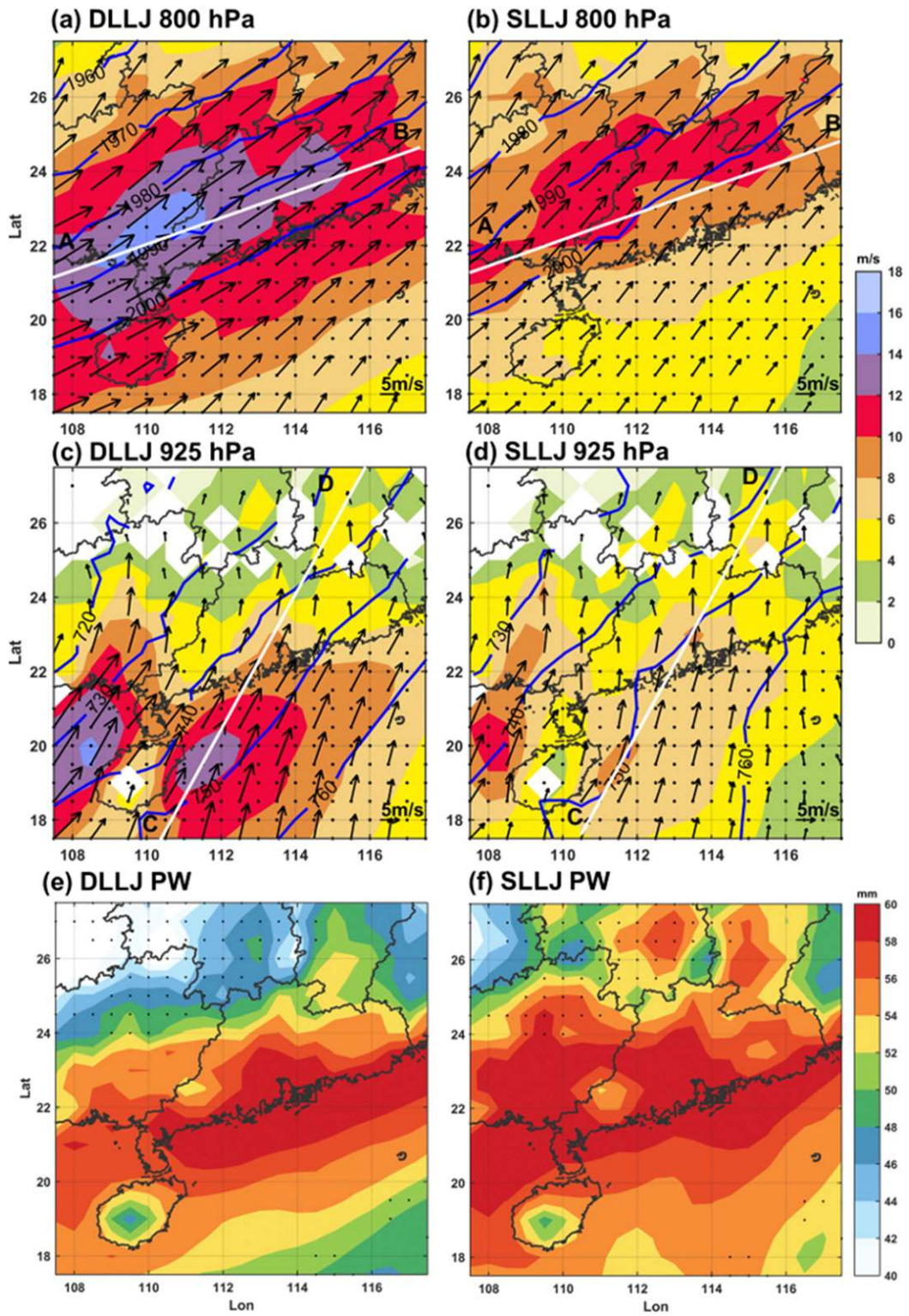
FIG. 9. As in Fig. 6, but for DLLJ-type and SLLJ-type warm-sector heavy rainfall episodes.
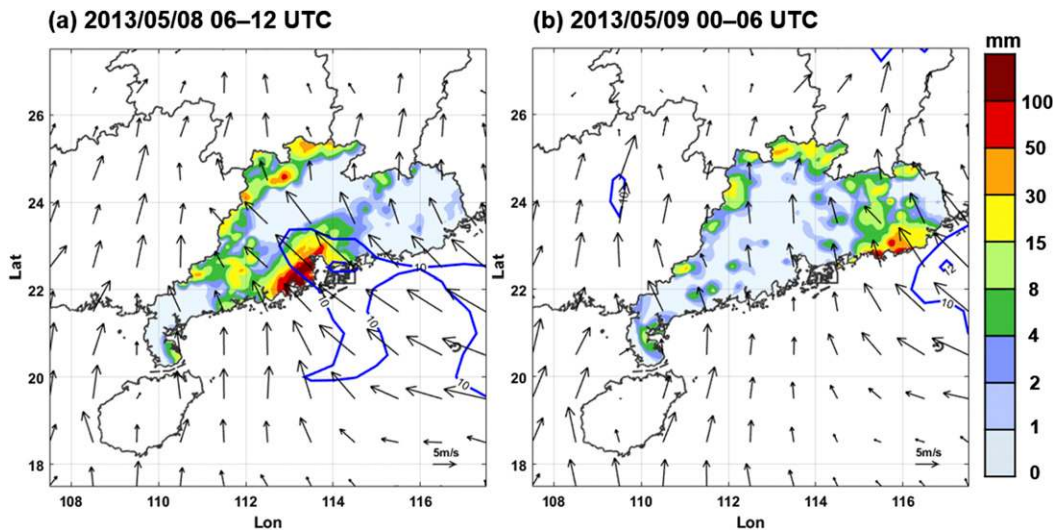
FIG. 10. Rainfall and 925-hPa LLJ distribution in the two BLJ-type episodes. The shadings are 6-h accumulated precipitation in Guangdong Province during (a) 0600–1200 UTC 8 May and (b) 0000–0600 UTC 9 May 2013. Also shown are the 925-hPa horizontal wind speeds over 10 m s^{-1} (contoured in blue every 2 m s^{-1}) and 925-hPa wind vectors at the start time of the rainfall episode from GFS analysis data. The referenced vector is given in the bottom right.

the same domain as in Fig. 1 at 800 and 925 hPa. The ME is defined as

$$ME = \frac{1}{n} \sum_{i=0}^{n} (X_i - Y_i),$$

where n is the total number of grid points, X_i is the WRF output, and Y_i is the GFS analysis variable at the same grid point. Considering the relatively small sample size of LLJ-type warm-sector heavy rainfall episodes (29, shown later in Table 1), the Spearman rank correlation R was applied to evaluate the magnitude of correlation between QPF skill (ETSs) and the ETSs of LLJ forecast, similar to Squitieri and Gallus (2016). The correlation R is defined as

$$R = 1 - \frac{6 \sum_{i=1}^{n} (x_i - y_i)^2}{n(n^2 - 1)},$$

where n is the sample size and x_i and y_i are the ranks of the variables to be correlated (Myers and Well 2003). Based on Table A10 of Conover (1971), for a sample size of 29, the 90% and 95% levels of statistical significance of the Spearman rank correlation are 0.2443 and 0.3113.

3. Results

a. General characteristics of warm-sector heavy rainfall

A total of 45 warm-sector heavy rainfall episodes in 2013 and 2014 were identified and classified into LLJ-type and no-LLJ-type episodes based on the criteria given in section 2, exhibiting distinct rainfall distributions. 64% of the warm-sector heavy rainfall episodes (29 episodes) were classified as the LLJ type (Table 1). Notably, there is still a considerable portion (36%) that is unassociated with LLJs, implying that the occurrence of an LLJ is not a necessary condition for warm-sector heavy rainfall in southern China. The composite 6-h accumulated precipitation in LLJ-type warm-sector heavy rainfall (Fig. 4a) is mainly concentrated along the coastline and the windward slope of mountains in central Guangdong Province (Fig. 1). The coastal lifting induced by the differential friction and the small hills is likely the primary cause for the strong coastal rainfall in the LLJ type (e.g., Colle and Yuter 2007; Chen et al. 2017), while the rainfall along the windward slope is probably due to windward inland terrain lifting. For the no-LLJ type (Fig. 4b), the accumulated precipitation is much smaller in amount and distributed relatively evenly over the inland region,[1] which could be attributable to the diurnal propagation of the land–sea-breeze fronts during low-wind days without LLJs (Chen et al. 2017; Wang and Sobel 2017).

---

[1] The statistical significance of the differences of accumulated precipitation, precipitable water, CAPE, horizontal wind speed, and horizontal convergence between composites were examined by either two-tailed Student's t test (same sample sizes) or two-tailed Welch's t test (different sample sizes) and the differences between composites discussed hereafter are significant at 90% level.
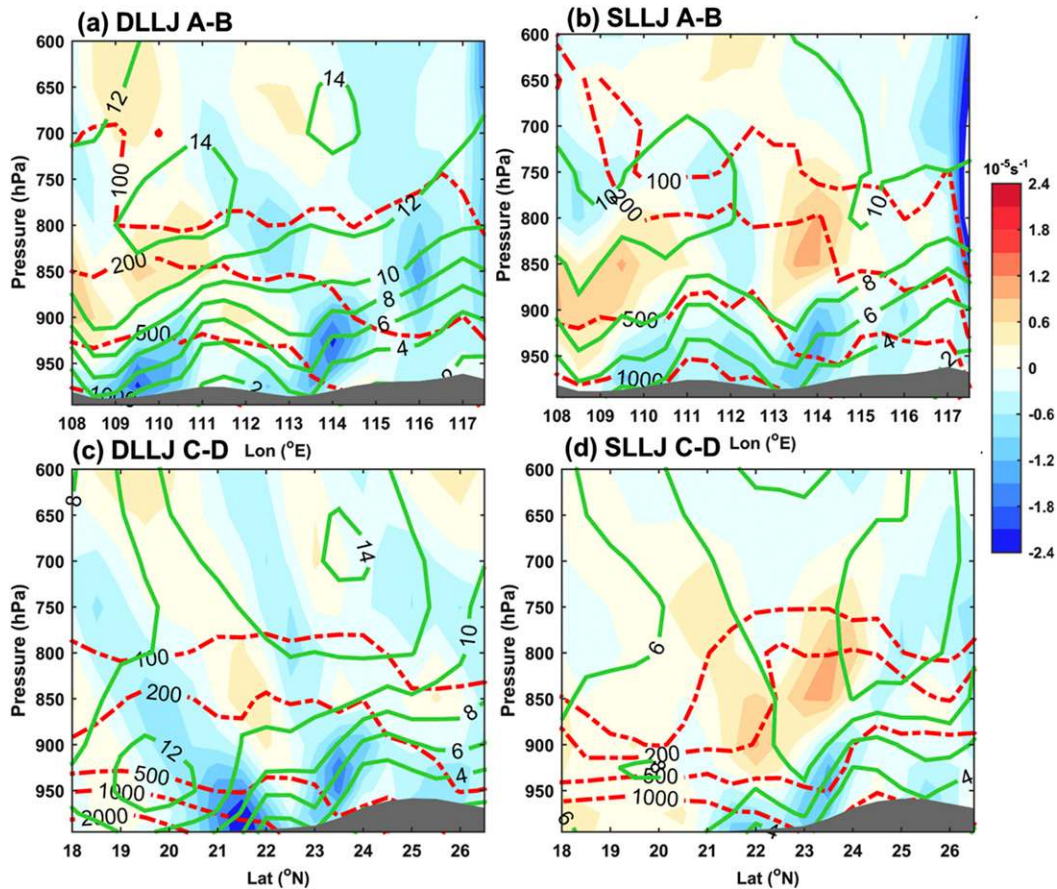
FIG. 11. Composite vertical cross sections at the start time of (a) DLLJ-type (path A–B in Fig. 9a) and (b) SLLJ-type (path A–B in Fig. 9b) warm-sector heavy rainfall episodes revealed by GFS analysis, including horizontal divergence (shaded every $0.3 \times 10^{-5}\,s^{-1}$), horizontal wind speed (contoured every $2\,m\,s^{-1}$ in bold green), and CAPE (contoured at 100, 200, 500, 1000, and 2000 J kg^{-1} in dashed red). (c),(d) As in (a),(b), but for the vertical cross sections along path C–D given in Figs. 9c and 9d.

The diurnal variation of the frequency of warm-sector heavy rainfall was further investigated. Generally, the warm-sector heavy rainfall in Guangdong Province presents a daytime peak over 1400–2000 LST, with a close second peak over 0800–1400 LST (Fig. 5a). The diurnal variation of the LLJ type is quite distinct from the no-LLJ type (Fig. 5b). The LLJ type peaks over 0800–1400 LST, which is earlier than the peak in the no-LLJ type (1400–2000 LST). Notably, the frequency over the early morning (0200–0800 LST) in the LLJ type is much higher than that in the no-LLJ type (Fig. 5b), which may be partly attributed to the diurnal variation of the BLJ (Du and Chen 2018) and the coastal convergence between the enhancing land breeze from evening to early morning and the strong southerly monsoonal flow (Chen et al. 2017). The composite synoptic environments at 800 and 925 hPa in the different types of warm-sector heavy rainfall are presented in Fig. 6. The composite environments were

obtained through averaging the weather variable fields from GFS analysis at the start time of the heavy rainfall episode (hereafter the same) to avoid as much as possible the contamination of convection, since the convection at the start time of most selected episodes is absent or relatively weak. In both types, southwesterly winds are dominant at 800 hPa (Figs. 6a,b) but are more southerly at 925 hPa (Figs. 6c,d). The low-level horizontal wind speed in the LLJ type (Figs. 6a,c) is significantly larger than that in the no-LLJ type (Figs. 6b,d). The 800-hPa jet stream core (>12 m s^{-1}) is located at the junction between Guangdong and Guangxi (Fig. 6a). At 925 hPa, there are two LLJs located in Beibu Gulf and the SCS, and the jet core in Beibu Gulf is stronger than that in the SCS (Fig. 6c). The dual-core LLJ at 925 hPa may be associated with the surface condition, and the friction over the island may lead to the weakening of the jet at 110°E and consequently the split in jet structure.
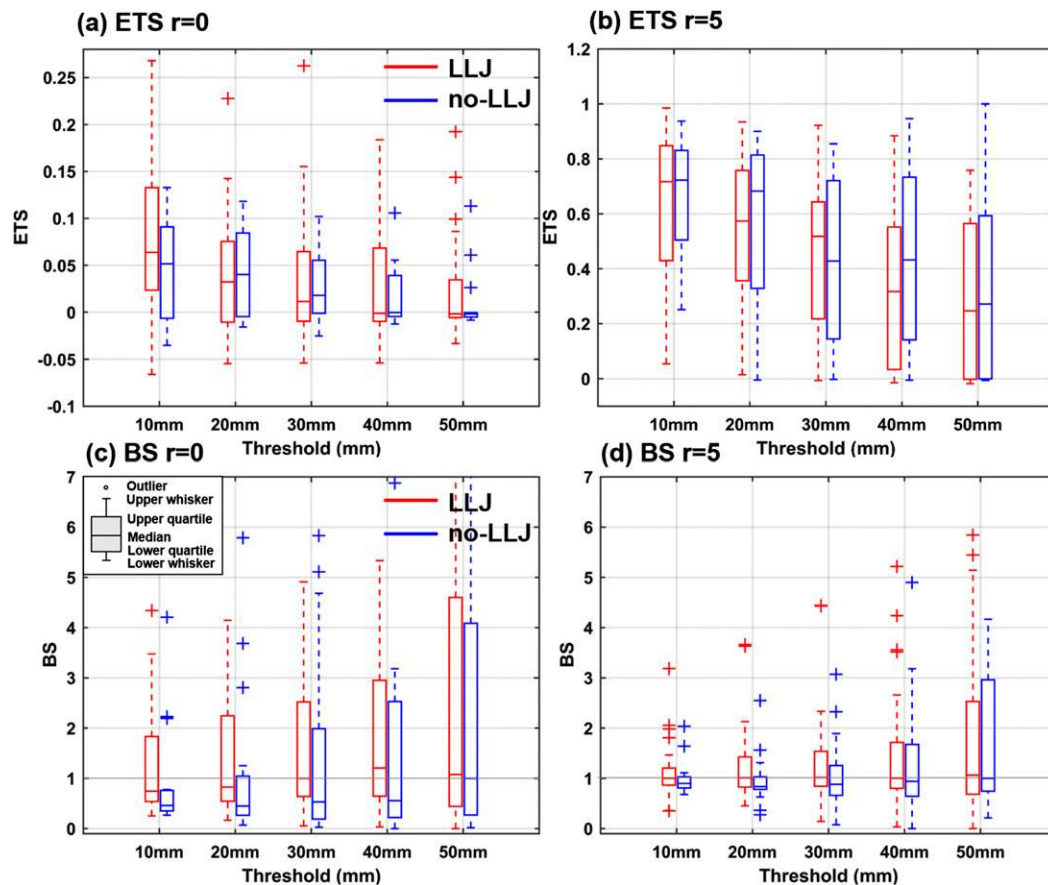
FIG. 12. Boxplots of (a) ETS and (c) BS of the 6-h QPF of WRF simulations in the LLJ-type (red) and no-LLJ-type (blue) episodes at different rainfall thresholds. (b),(d) As in (a),(c), but for the neighborhood-based ETS and BS with a radius of influence of 0.5° ($r = 5$). The gray line in (c),(d) denotes a BS of 1. The plotting style for all box-and-whisker plots is exemplified in (c). The whiskers extend to the most extreme data points that are not considered outliers. Points are identified as outliers if they are larger than $q_3 + 1.5(q_3 - q_1)$ or smaller than $q_1 - 1.5(q_3 - q_1)$, where q_1 and q_3 are the 25th and 75th percentiles (same for the boxplots hereafter).

In addition, the precipitable water in LLJ type (Fig. 6e) is significantly larger than that in no-LLJ type (Fig. 6f) over the southeastern coastal region, which may be due to stronger moisture transport in LLJ type.

Besides horizontal differences, the LLJ type also differs from the no-LLJ type in the vertical structure of the dynamic and thermodynamic environments. Composite vertical cross sections were taken along the axis of SLLJ (path A–B given in Fig. 6a) and the axis of BLJ (path C–D given in Fig. 6c) for both the LLJ type and no-LLJ type (Fig. 7). The magnitudes of the horizontal wind speed and associated divergence are generally larger in the LLJ type than in the no-LLJ type. In the LLJ type, there is a jet core near 800 hPa over 109°–111°E in the cross section along the axis of SLLJ (Fig. 7a), which is consistent with the location of SLLJ shown in Fig. 2b.

The convergence near 113°–114°E corresponds to the inland heavy rainfall shown in Fig. 4a. Notably, this convergence is at ~925 hPa and not quite relevant to the terminus of SLLJ (near ~112°E) but rather seems more like a result of windward inland terrain lifting near 925 hPa, which indicates that the terminus of SLLJ may not directly contribute to the inland heavy rainfall. The cross section along the axis of BLJ in LLJ type (Fig. 7c) reveals a jet core near 925 hPa over 19°–20.5°N which is consistent with the location of BLJ shown in Fig. 2b. There is large convergence (~$1.8 \times 10^{-5}\,\mathrm{s}^{-1}$) over the coastal region and the inland windward slope below 900 hPa in the LLJ type (Fig. 7c), which corresponds to the large rainfall accumulation over these two regions (Fig. 4a). The drastic decline of the wind speed due to differential friction near the coast and the lifting of inland mountains (Fig. 7c) is conducive to the convergence.
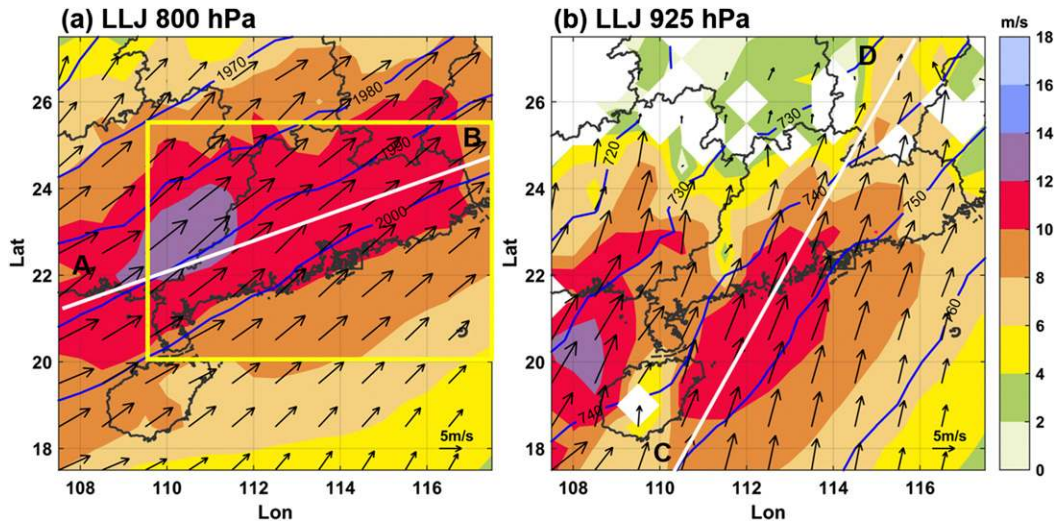
FIG. 13. Composite low-level synoptic environment at the start time of LLJ-type warm-sector heavy rainfall episodes revealed by WRF simulations, including geopotential height (contoured in blue every 10 gpm), horizontal wind speed (shaded every $2 \, \mathrm{m \, s^{-1}}$), and wind vector at (a) 800 and (b) 925 hPa. The referenced vector is given in the bottom right. The yellow box denotes the same domain as in Fig. 1. The paths for the vertical cross sections in Fig. 16 are given as the bold white lines.

The coastal convergence is stronger than the inland convergence (Fig. 7c), which is consistent with the larger intensity of coastal rainfall in Fig. 4a. In addition, the near-surface CAPE over coastal region (22°N in path C–D) in LLJ type (Fig. 7c) is significantly larger than that in no-LLJ type (Fig. 7d), which is favorable for the heavy coastal rainfall in LLJ type. Over the inland region (111°–115°E in path A–B), the CAPE below 900 hPa in no-LLJ type (Fig. 7b) is generally larger than LLJ type

(Fig. 7a), which might contribute to more widely distributed inland precipitation in no-LLJ type.

b. LLJ-type warm-sector heavy rainfall

The LLJ-type warm-sector heavy rainfall episodes were further classified into DLLJ, SLLJ, and BLJ types, as described in section 2b. Among the 29 LLJ-type episodes, there are 21 DLLJ-type episodes, 6 SLLJ-type episodes, and 2 BLJ-type episodes
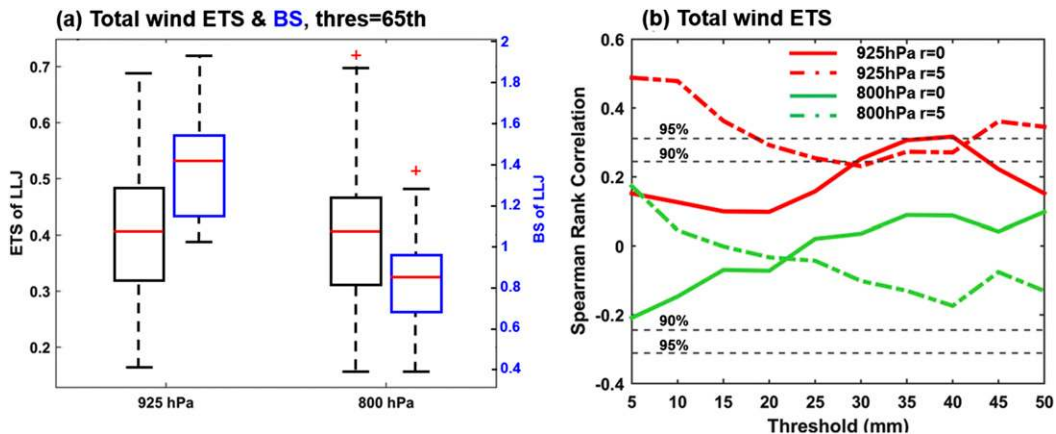

FIG. 14. LLJ forecast accuracy and its correlation with ETSs of precipitation. (a) The boxplots of the ETS (black) and BS (blue) of LLJ at 800 and 925 hPa at the start time of LLJ-type episodes over the domain shown in Fig. 6. (b) Spearman rank correlations between the 6-h QPF $ETS_{r=0}$ (solid) and $ETS_{r=5}$ (dashed) at 5–50 mm thresholds in the LLJ type and ETSs of total wind at 800 and 925 hPa at the start time of LLJ-type episodes over the domain shown in Fig. 6. The outer black lines in (b) delineate the statistically significant Spearman rank correlation value as a function of sample size at the 95% confidence interval of rejecting the null hypothesis as defined in Conover (1971). The inner black lines in (b) are for the 90% confidence interval.

(Table 1), suggesting that it is more common for the LLJ at 800 and 925 hPa to exist simultaneously during warm-sector heavy rainfall. Considering the small sample size in the BLJ type, only the DLLJ and SLLJ types were examined through composite analyses. The composite 6-h accumulated precipitation distribution in the DLLJ type (Fig. 8a) greatly resembles that in the LLJ type, which reconfirms the dominant percentage of the DLLJ type. With weak precipitation over the coastal region, the SLLJ type is characterized by strong precipitation over the inland mountainous region (Fig. 8b), which is probably due to the windward lifting of inland mountains. The horizontal wind speed in the DLLJ type is significantly larger than in the SLLJ type at both pressure levels (Fig. 9). In the DLLJ type, the LLJs are distributed similarly as in the LLJ-type but with stronger and wider jet streams (Figs. 9a,c). The SLLJ has its main core over Beibu Gulf and eastern Guangxi Province and its northern end over the northeastern Guangdong Province (Fig. 9a). This composite pattern of LLJs in the DLLJ type is different from the double-LLJ pattern in Du and Chen (2019), where the core of SLLJ was located to the north of Guangdong, making the entrance of the SLLJ perfectly situated over the terminus of the BLJ. In the SLLJ type, the jet stream at 800 hPa (Fig. 9b) extends from eastern Guangxi to northeastern Guangdong and the LLJ over the SCS at 925 hPa is absent (Fig. 9d). For both of the two BLJ type episodes, the rainfall is concentrated along the coast and influenced by strong southeasterly winds in the boundary layer (Fig. 10), indicating a close relationship between the BLJ and coastal heavy rainfall. Notably, there is no significant difference in precipitable water between DLLJ and SLLJ type over Guangdong Province and SCS (Figs. 9e,f), indicating that the moisture condition is relatively similar between these two types of warm-sector heavy rainfall.

Similarly, a composite vertical cross section was taken for the DLLJ type (path given in Figs. 9a,c) and SLLJ type (path given in Figs. 9b,d) (Fig. 11). In the DLLJ type, the jet structure and associated horizontal divergence resemble those in the LLJ type with stronger intensity. In the SLLJ type, the large-wind core over the offshore region along path C–D (Fig. 11d) is weaker than the DLLJ type (Fig. 11c) by ~4 m s^{-1}. As a result, the near-surface convergence over coastal region was much smaller (Figs. 11c,d), which may have led to its absence of coastal rainfall accumulation. However, the CAPE below 900 hPa over inland region in Guangdong Province (111°–115°E in path A–B) in SLLJ type (Fig. 11b) is larger than that in DLLJ type, which suggests a more
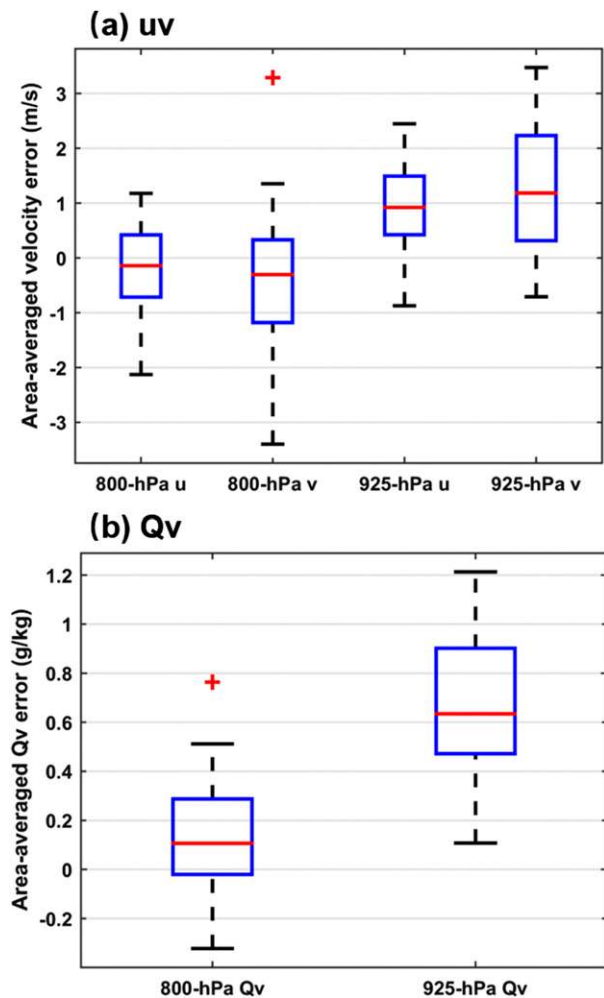

FIG. 15. Boxplots of MEs of the (a) wind component and (b) water vapor mixing ratio at 800 and 925 hPa at the start time of the LLJ-type episodes over the yellow box given in Fig. 13a (same domain as in Fig. 1). The plotting style for all box-and-whisker plots is exemplified in Fig. 12c.

favorable thermodynamic environment for heavy rainfall over inland region.

To summarize, as the dominant type of warm-sector heavy rainfall, the LLJ type is distinguished by extreme rainfall accumulation over the southern coastal region and is commonly accompanied by LLJs at both 800 and 925 hPa. Located near the terminus of the offshore LLJ over the SCS at 925 hPa, the heavy rainfall in the coastal region is closely related to the coastal convergence below ~900 hPa.

c. WRF simulation evaluation

WRF simulations severely underestimate the rainfall in both the LLJ and no-LLJ types with a worse performance in the LLJ type (Fig. 4). The heavy rainfall over the coastal region in the LLJ type is generally
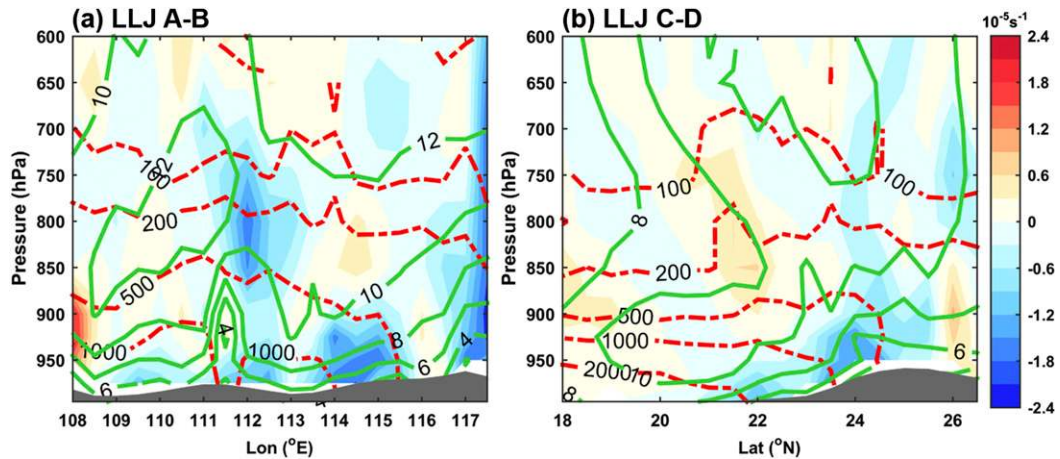
FIG. 16. Composite vertical cross sections at the start time of LLJ-type warm-sector heavy rainfall episodes revealed by WRF simulations along (a) path A–B (given in Fig. 13a) and (b) path C–D (given in Fig. 13b), including horizontal divergence (shaded every $0.3 \times 10^{-5} \, \mathrm{s}^{-1}$), horizontal wind speed (contoured every $2 \, \mathrm{m \, s}^{-1}$ in bold green), and CAPE (contoured at 100, 200, 500, 1000, and $2000 \, \mathrm{J \, kg}^{-1}$ in dashed red).

underestimated (Figs. 4a,c), while the inland rainfall distribution in the no-LLJ type is captured decently (Figs. 4b,d). In terms of the median, both $ETS_{r=0}$ and $ETS_{r=5}$ at 10–50 mm in the LLJ type are lower than that in the no-LLJ type (except for $ETS_{r=0}$ at 10 mm and $ETS_{r=5}$ at 30 mm) (Figs. 12a,b), indicating the overall better rainfall simulation in the no-LLJ type. The ETSs of precipitation simulations gradually decrease with increasing thresholds and the forecast skill is nearly lost at 50 mm for both types without applying neighborhood verification (Fig. 12a). The medians of the BS are all smaller than 1 (Figs. 12c,d) in no-LLJ type, while they are generally smaller than 1 in LLJ type except for an overestimation at higher thresholds ($BS_{r=0}$ at 40 and 50 mm and $BS_{r=5}$ at 50 mm), suggesting that convection-permitting WRF simulations underestimate the light rainfall in both LLJ type and no-LLJ type.

The WRF simulations of LLJ-type episodes were further examined because of their higher frequency but relatively poor forecast skill. In general, WRF simulations underestimate the 800-hPa wind speed but overestimate the 925-hPa wind speed and low-level moisture over the region of focus during LLJ-type warm-sector heavy rainfall episodes. At 800 hPa, the simulated LLJ has a similar location but is weaker compared with GFS analysis data (Fig. 13a and Fig. 6a); at 925 hPa, WRF simulations reproduce the observed double LLJs as shown in Fig. 6c with a weaker jet over Beibu Gulf and a more-to-the-north jet over the SCS (Fig. 13b).

ETSs, BSs, and MEs were calculated to evaluate the forecast errors of LLJs quantitatively. Results show that the forecast accuracy of jet stream on the two pressure

levels are comparable according to their similar ETSs (Fig. 14a). However, the strength of the jet on 925 hPa is overestimated with the median of BS higher than 1 while the intensity of the jet on 800 hPa is underestimated, to a smaller extent relative to that of the overestimation on 925 hPa, with the median of BS lower than 1 (Fig. 14a). This feature is confirmed further in the MEs of the horizontal wind component at 800 and 925 hPa (Fig. 15a) over the yellow box in Fig. 13 (the same domain as Fig. 1) at the start time of each LLJ-type episode. Results show that the horizontal wind speed is underestimated at 800 hPa but more seriously overestimated at 925 hPa in terms of the median ME, which is particularly true for the 925-hPa v component (with a median ME of $1.18 \, \mathrm{m \, s}^{-1}$). These results corroborate the weaker jet at 800 hPa and more-to-the-north jet over the SCS at 925 hPa exhibited in the WRF simulations (Fig. 13). The simulated low-level moisture is overall higher than that of the GFS analysis, with a median ME of $0.11 \, \mathrm{g \, kg}^{-1}$ at 800 hPa and $0.63 \, \mathrm{g \, kg}^{-1}$ at 925 hPa (Fig. 15b).

The severe underestimation of the coastal rainfall in the LLJ-type WRF simulations might mainly be attributable to the north bias of the offshore LLJ over the SCS at 925 hPa. As shown in the simulated LLJ-type composite vertical cross section along SLLJ axis (Fig. 16a; path given in Fig. 13a), the jet core near ~800 hPa over 109°–111°E is weaker and the inland convergence near 114°E in the simulation is more to the east compared with GFS analysis (Fig. 7a). In the vertical cross section along the BLJ axis (Fig. 16b; path given in Fig. 13b), the offshore jet core near ~925 hPa in the simulation is stronger and shifted to

the north with an increment of $2\,\mathrm{m\,s}^{-1}$ in inland wind speed over 20.5°–22.5°N below ~900 hPa compared with GFS analysis (Fig. 7c). With the northern intrusion of the BLJ, the horizontal wind speed gradient near the coastal region is greatly weakened, which eventually leads to the underestimation of coastal convergence over 20.5°–22.5°N and the associated heavy rainfall. Due to the low-level moisture overestimation, the simulated CAPE over the region of interest is generally larger than that in GFS analysis in both cross sections, indicating a more beneficial thermodynamic environment in WRF simulations for heavy rainfall. However, even with higher CAPE, the heavy rainfall along the coast is still underestimated due to the lack of dynamic convergence.

Further evidence on the relation between the forecast accuracy of BLJ with the QPF skills of warm-sector heavy rainfall in southern China was found by calculating the Spearman correlation coefficient between 6-h QPF ETSs in LLJ type episodes and ETSs$_{r=0}$ of the LLJ at the start time of the LLJ-type episodes (Fig. 14b). Results show the most significant correlation between the ETS of total wind on 925 hPa and the ETS$_{r=5}$ of precipitation. Higher ETS of total wind on 925 hPa is significantly correlated with higher ETS$_{r=5}$ of precipitation, while there is no significant correlation between ETS of total wind on 800 hPa and ETS of precipitation (Fig. 14b). These results demonstrate that the forecast accuracy of BLJ is the most significantly correlated with the QPF skills of warm-sector heavy rainfall in southern China.

Notably, the simulated coastal rainfall maximum shifts to west to around 21.5°N, 111.5°E near Yangjiang City compared with the observation. This shift may be attributed to the forecast errors of both the near-surface convergence associated with BLJ and precipitable water. On the one hand, the 975-hPa convergence at 22°N, 113°–114°E, where the heavy coastal rainfall maximum occurs in the observation, is weaker in simulation due to the northern intrusion of BLJ (Fig. 17b) compared with GFS analysis (Fig. 17a); on the other hand, at 21.5°N, 111.5°E, the near-surface convergence in simulation is similar but the precipitable water is larger than GFS analysis by ~4 mm, which may have helped the simulated coastal rainfall maximum shift to the west. Furthermore, since southerly wind is stronger in the simulation, the lifting by mountains near the simulated rainfall maximum may have played an important role, too.

The WRF simulations of the DLLJ type generally resembles those of the LLJ type. As shown in Figs. 8a and 8c, the heavy rainfall over the coastal region in the DLLJ type is nearly missed in the WRF simulations.
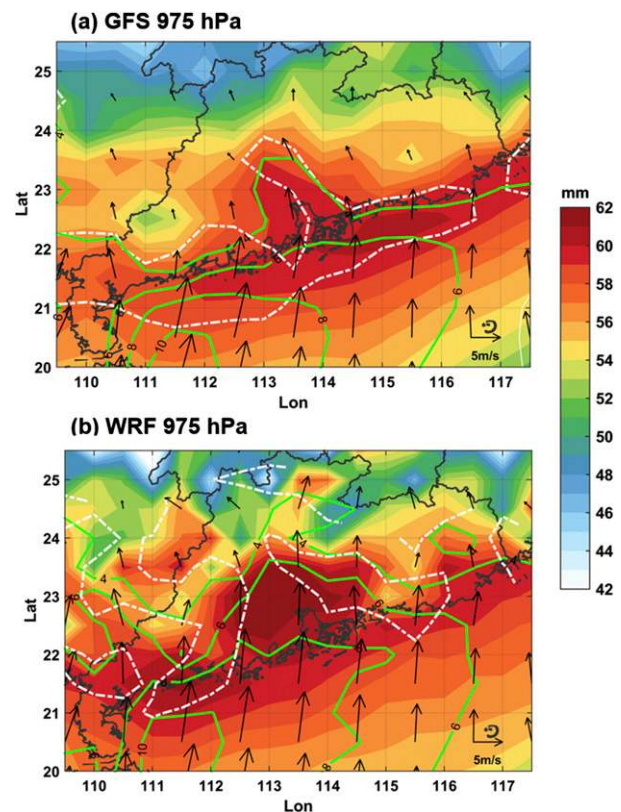

FIG. 17. Composite horizontal wind speed (contoured in green every $2\,\mathrm{m\,s}^{-1}$), horizontal divergence of $-1 \times 10^{-5}\,\mathrm{s}^{-1}$ (contoured in dashed white), horizontal wind vector at 975 hPa, and precipitable water (shaded every 1 mm) at the start time of LLJ-type episodes in (a) GFS analysis and (b) WRF simulations.

Similar to the LLJ type, the absence of coastal rainfall is associated with the north bias of the simulated 925-hPa LLJ over the SCS. Compared with the GFS analysis results, the simulated jet core at ~800 hPa (Figs. 19a and 11a) and the simulated jet stream at 800 hPa (Figs. 18a and 9a) are weaker. The north bias of the simulated 925-hPa LLJ over the SCS in the DLLJ type is even more apparent than that in the LLJ type, with the high-wind region (over $10\,\mathrm{m\,s}^{-1}$) intruding into Guangdong Province (Fig. 18c) and the jet core at ~925 hPa moving toward the coastal region (Fig. 19c), which is consistent with the positive ME of the 925-hPa wind mentioned earlier. As a result of the north bias of the 925-hPa LLJ, the inland southerly winds below ~900 hPa are overpredicted (Figs. 19c and 11c), which eventually leads to the underestimation of coastal convergence and associated heavy rainfall.

The inland rainfall maxima in the SLLJ type are overpredicted over a wider inland region (Figs. 8b,d). At 800 hPa, the simulated jet stream is narrower and weaker than in the GFS analysis (Figs. 18b and 9b). At 925 hPa, the LLJ over Beibu Gulf is reproduced by
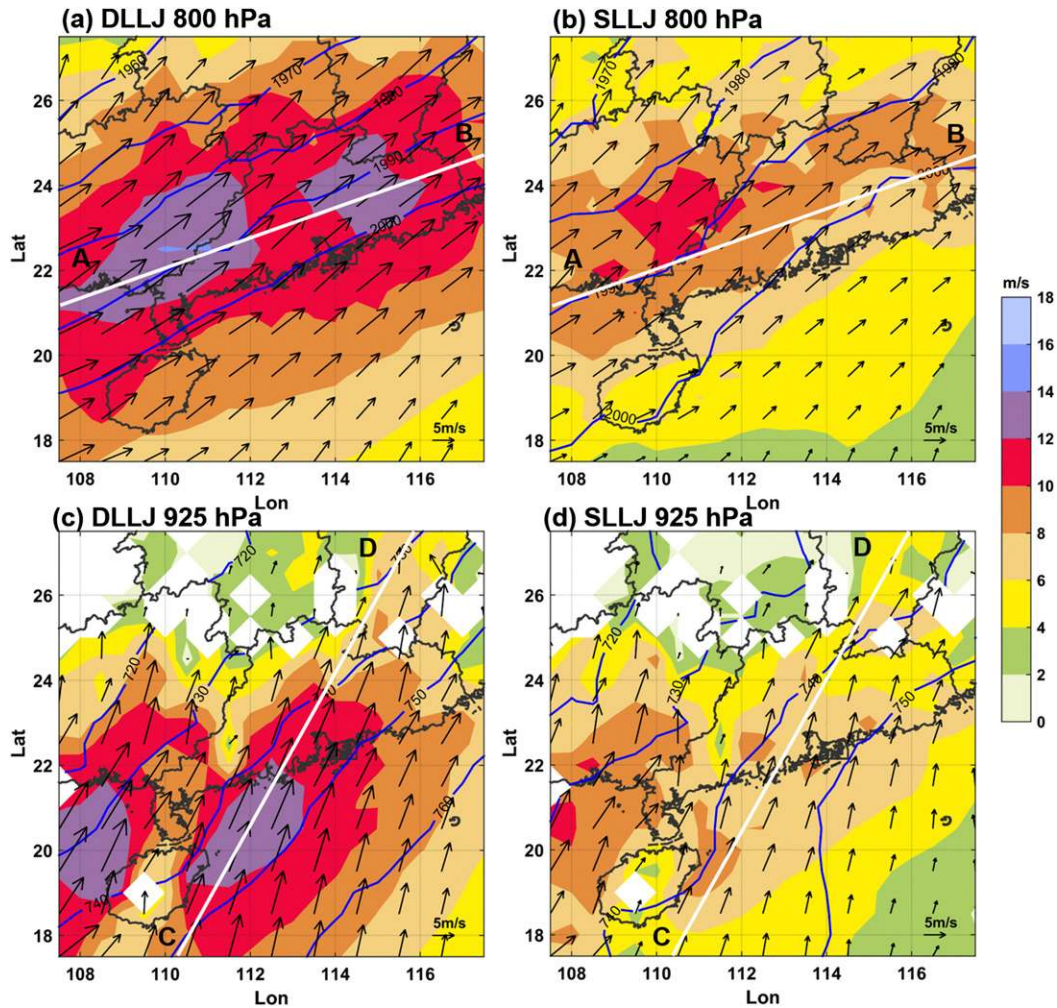
FIG. 18. As in Figs. 9a–d, but for WRF simulations.

WRF with comparable intensity (Figs. 18d and 9d), and the LLJ over the SCS is absent, similar to in the GFS analysis. For both DLLJ and SLLJ types, CAPE below ~900 hPa is generally larger in WRF simulations (Fig. 19) compared with GFS analysis (Fig. 11), indicating a more favorable thermodynamic environment. The overestimation of water vapor mixing ratio at low levels shown in Fig. 15 may have contributed to the larger CAPE in WRF simulations.

4. Conclusions

In the present study, a total of 45 warm-sector heavy rainfall episodes in 2013 and 2014 over Guangdong Province in southern China were identified and classified into LLJ-type and no-LLJ-type episodes based on their relationship with LLJs. The LLJ-type episodes account for 64% and are characterized by heavy rainfall along the southern coast and the windward slope of

the mountains in central Guangdong, which is associated with the coastal lifting induced by differential friction and windward lifting of inland mountains. The no-LLJ-type episodes account for 36%, and feature generally smaller rainfall amounts and a relatively even distribution over the inland region. Compared with the no-LLJ type, LLJ-type episodes have a much higher frequency in the early morning (0200–0800 LST), which may be associated with the diurnal variation of BLJ and coastal convergence between the enhancing land breeze from evening to early morning and the strong southerly monsoonal flow.

Composite analyses reveal distinct environments in the different types of warm-sector heavy rainfall. Although both the LLJ and no-LLJ types occur under low-level southwesterly winds, the low-level horizontal wind speeds in the LLJ type are much larger than those in the no-LLJ type. In the LLJ type, the 800-hPa LLJ core is located at the junction between Guangdong
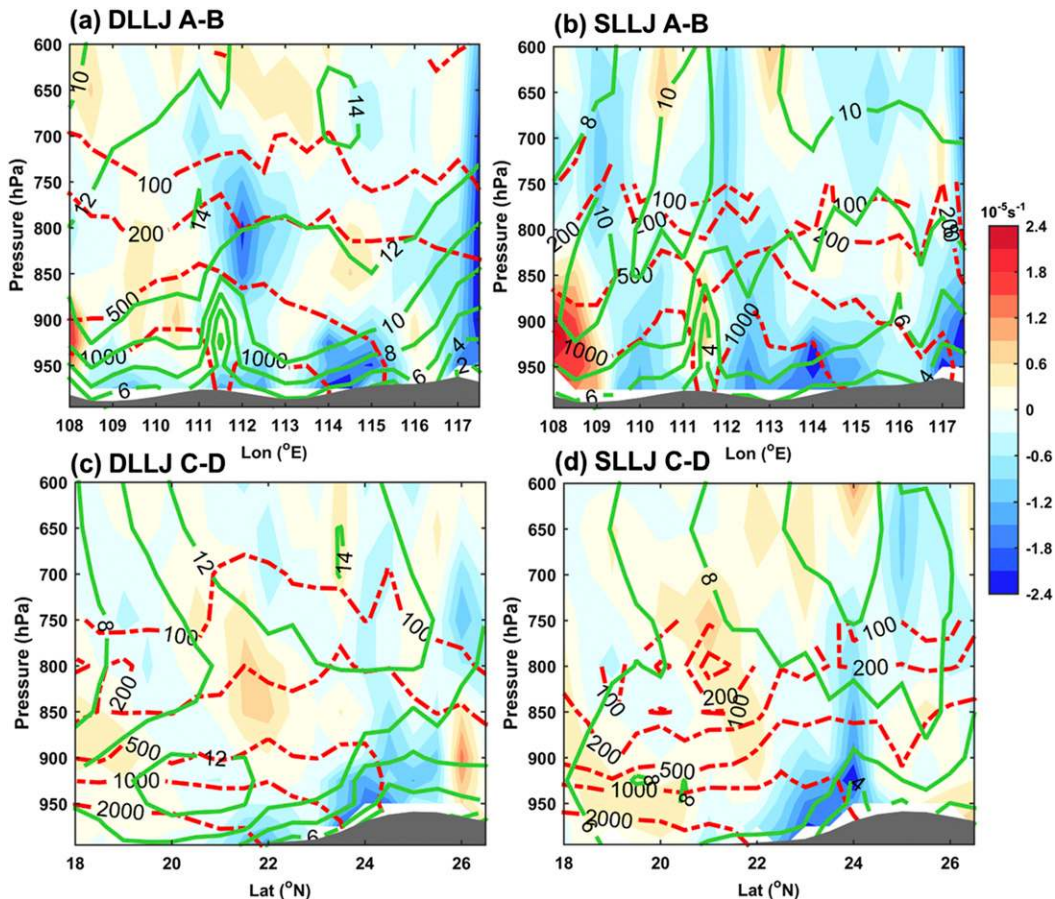
FIG. 19. As in Fig. 11, but for WRF simulations.

and Guangxi Provinces, while at 925 hPa there are two LLJs, over Beibu Gulf and the SCS, respectively. Vertically, two large wind speed cores are observed over the offshore region at ~925 hPa and to the west of Guangdong at ~800 hPa, which correspond to the BLJ and SLLJ. The drastic decline of the onshore winds below 900 hPa because of differential friction near the coast and the blocking of inland mountains, result in strong convergence over the coastal region and the inland windward slope in the LLJ type, which is consistent with the large rainfall accumulation over these two regions. The thermodynamic environment in the LLJ type is characterized by more sufficient precipitable water and stronger conditional instability over coastal region, which is conducive to the overall stronger coastal rainfall in the LLJ type warm-sector heavy rainfall.

The LLJ-type warm-sector heavy rainfall episodes were further divided into 21 DLLJ-type, 6 SLLJ-type, and 2 BLJ-type episodes, indicating the common occurrence of an LLJ at both 800 and 925 hPa during warm-sector heavy rainfall in southern China. The rainfall and LLJ distributions in the DLLJ type resemble those of the LLJ type; whereas, in the SLLJ type, the coastal rainfall is greatly weakened, which is probably due to the lack of coastal convergence associated with the absence of a 925-hPa LLJ over the SCS.

WRF simulations of all the identified warm-sector heavy rainfall episodes and associated LLJs were evaluated. Convection-permitting WRF simulations present lower ETSs in the LLJ type than in the no-LLJ type, since the heavy rainfall over the coastal region in the LLJ type is severely underestimated. The QPF skill of the LLJ-type warm-sector heavy rainfall is significantly correlated with the forecast accuracy of LLJs, especially the accuracy of 925-hPa winds. The WRF simulations generally overestimate the 925-hPa wind speed and the moisture at both pressure levels, but slightly underestimate the 800-hPa wind speed. The heavy rainfall along the coast in the LLJ type (especially in the DLLJ type) is severely underestimated in the WRF simulations, which could mainly be attributed to the north bias of the offshore LLJ over the SCS at 925 hPa. With the northern intrusion of the strong BLJ, the horizontal wind speed gradient near the coastal region is weakened, which

eventually leads to the underestimation of coastal convergence and associated heavy rainfall.

The present research pinpoints that the major deficiency of WRF simulations of warm-sector heavy rainfall in southern China is the severe underestimation of coastal rainfall, which is closely related to the positive bias of horizontal wind within the boundary layer over the inland coastal region. Within the specific regime in southern China, the positive inland wind bias is likely to be associated with the insufficient contrast of the roughness between land and ocean and lack of subgrid-scale terrain influence in the numerical model, which is worth investigating in a future study.

REFERENCES

Barthold, F. E., T. E. Workoff, B. A. Cosgrove, J. J. Gourley, D. R. Novak, and K. M. Mahoney, 2015: Improving flash flood forecasts: The HMT-WPC Flash Flood and Intense Rainfall Experiment. *Bull. Amer. Meteor. Soc.*, **96**, 1859–1866, https://doi.org/10.1175/BAMS-D-14-00201.1.

Chen, G., R. Lan, W. Zeng, H. Pan, and W. Li, 2018: Diurnal variations of rainfall in surface and satellite observations at the monsoon coast (South China). *J. Climate*, **31**, 1703–1724, https://doi.org/10.1175/JCLI-D-17-0373.1.

Chen, G. T. J., and C. C. Yu, 1988: Study of low-level jet and extremely heavy rainfall over northern Taiwan in the mei-yu season. *Mon. Wea. Rev.*, **116**, 884–891, https://doi.org/10.1175/1520-0493(1988)116<0884:SOLLJA>2.0.CO;2.

Chen, Q., 1982: The instability of the gravity-inertia wave and its relation to low-level jet and heavy rainfall. *J. Meteor. Soc. Japan*, **60**, 1041–1057, https://doi.org/10.2151/jmsj1965.60.5_1041.

Chen, X., K. Zhao, M. Xue, B. Zhou, X. Huang, and W. Xu, 2015: Radar-observed diurnal cycle and propagation of convection over the Pearl River Delta during Mei-Yu season. *J. Geophys. Res. Atmos.*, **120**, 12 557–12 575, https://doi.org/10.1002/2015JD023872.

——, F. Zhang, and K. Zhao, 2016: Diurnal variations of the land–sea breeze and its related precipitation over South China. *J. Atmos. Sci.*, **73**, 4793–4815, https://doi.org/10.1175/JAS-D-16-0106.1.

——, ——, and ——, 2017: Influence of monsoonal wind speed and moisture content on intensity and diurnal variations of the mei-yu season coastal rainfall over South China. *J. Atmos. Sci.*, **74**, 2835–2856, https://doi.org/10.1175/JAS-D-17-0081.1.

Chen, Y.-L., X. A. Chen, and Y.-X. Zhang, 1994: A diagnostic study of the low-level jet during TAMEX IOP 5. *Mon. Wea. Rev.*, **122**, 2257–2284, https://doi.org/10.1175/1520-0493(1994)122<2257:ADSOTL>2.0.CO;2.

Chien, F.-C., and B. J.-D. Jou, 2004: MM5 ensemble mean precipitation in the Taiwan area for three early summer convective

(mei-yu) seasons. *Wea. Forecasting*, **19**, 735–750, https://doi.org/10.1175/1520-0434(2004)019<0735:MEMPFI>2.0.CO;2.

Clark, A. J., W. A. Gallus Jr., and M. L. Weisman, 2010: Neighborhood-based verification of precipitation forecasts from convection-allowing NCAR WRF model simulations and the operational NAM. *Wea. Forecasting*, **25**, 1495–1509, https://doi.org/10.1175/2010WAF2222404.1.

Colle, B. A., and S. E. Yuter, 2007: The impact of coastal boundaries and small hills on the precipitation distribution across southern Connecticut and Long Island, New York. *Mon. Wea. Rev.*, **135**, 933–954, https://doi.org/10.1175/MWR3320.1.

Conover, W. J., 1971: *Practical Nonparametric Statistics.* 3rd ed. John Wiley and Sons, 542 pp.

Ding, Y. H., 1994: *Monsoons over China.* Kluwer Academic Publishers, 419 pp.

Ding, Z., C. Liu, and X. Shen, 2011: Statistical analysis of the relationship among warm sector heavy rainfall, upper and lower tropospheric jet stream and south Asia high in May and June from 2005 to 2008. *J. Trop. Meteor.*, **27** (3), 307–316.

Du, Y., and G. Chen, 2018: Heavy rainfall associated with double low-level jets over southern China. Part I: Ensemble-based analysis. *Mon. Wea. Rev.*, **146**, 3827–3844, https://doi.org/10.1175/MWR-D-18-0101.1.

——, and ——, 2019: Heavy rainfalls associated with double low-level jets over southern China. Part II: Convection initiation. *Mon. Wea. Rev.*, **147**, 543–565, https://doi.org/10.1175/MWR-D-18-0102.1.

——, Q. H. Zhang, Y. Yue, and Y. M. Yang, 2012: Characteristics of low-level jets in Shanghai during the 2008–2009 warm seasons as inferred from wind profiler radar data. *J. Meteor. Soc. Japan*, **90**, 891–903, https://doi.org/10.2151/jmsj.2012-603.

——, Q. Zhang, Y. Chen, Y. Zhao, and X. Wang, 2014: Numerical simulations of spatial distributions and diurnal variations of low-level jets in China during early summer. *J. Climate*, **27**, 5747–5767, https://doi.org/10.1175/JCLI-D-13-00571.1.

——, Y.-L. Chen, and Q. Zhang, 2015: Numerical simulations of the boundary layer jet off the southeastern coast of China. *Mon. Wea. Rev.*, **143**, 1212–1231, https://doi.org/10.1175/MWR-D-14-00348.1.

Dudhia, J., 1989: Numerical study of convection observed during the Winter Monsoon Experiment using a mesoscale two-dimensional model. *J. Atmos. Sci.*, **46**, 3077–3107, https://doi.org/10.1175/1520-0469(1989)046<3077:NSOCOD>2.0.CO;2.

Ebert, E. E., 2008: Fuzzy verification of high-resolution gridded forecasts: A review and proposed framework. *Meteor. Appl.*, **15**, 51–64, https://doi.org/10.1002/met.25.

Grell, G. A., and D. Devenyi, 2002: A generalized approach to parameterizing convection combining ensemble and data assimilation techniques. *Geophys. Res. Lett.*, **29**, 1693, https://doi.org/10.1029/2002GL015311.

He, L., T. Chen, and Q. Kong, 2016: A review of studies on prefrontal torrential rain in South China (in Chinese with English abstract). *J. Appl. Meteor. Sci.*, **27** (5), 559–569.

Hong, S.-Y., J. Dudhia, and S.-H. Chen, 2004: A revised approach to ice microphysical processes for the bulk parameterization of clouds and precipitation. *Mon. Wea. Rev.*, **132**, 103–120, https://doi.org/10.1175/1520-0493(2004)132<0103:ARATIM>2.0.CO;2.

——, Y. Noh, and J. Dudhia, 2006: A new vertical diffusion package with an explicit treatment of entrainment processes. *Mon. Wea. Rev.*, **134**, 2318–2341, https://doi.org/10.1175/MWR3199.1.

Huang, L., and Y. Luo, 2017: Evaluation of quantitative precipitation forecasts by TIGGE ensembles for south China

during the presummer rainy season. *J. Geophys. Res. Atmos.*, **122**, 8494–8516, https://doi.org/10.1002/2017JD026512.

Huang, S. S., 1986: *Heavy Rainfall over Southern China in the Pre-Summer Rainy Season* (in Chinese). Guangdong Science and Technology Press, 244 pp.

Jolliffe, I. T., and D. B. Stephenson, 2003: *Forecast Verification: A Practitioner's Guide in Atmospheric Science*. Wiley and Sons, 240 pp.

Kalnay, E., M. Kanamitsu, and W. E. Baker, 1990: Global numerical weather prediction at the National Meteorological Center. *Bull. Amer. Meteor. Soc.*, **71**, 1410–1428, https://doi.org/10.1175/1520-0477(1990)071<1410:GNWPAT>2.0.CO;2.

Kleist, D. T., D. F. Parrish, J. C. Derber, R. Treadon, W. S. Wu, and S. Lord, 2009: Introduction of the GSI into the NCEP global data assimilation system. *Wea. Forecasting*, **24**, 1691–1705, https://doi.org/10.1175/2009WAF2222201.1.

Luo, Y., H. Wang, R. Zhang, W. Qian, and Z. Luo, 2013: Comparison of rainfall characteristics and convective properties of monsoon precipitation systems over south China and the Yangtze and Huai River basin. *J. Climate*, **26**, 110–132, https://doi.org/10.1175/JCLI-D-12-00100.1.

——, and Coauthors, 2017: The Southern China Monsoon Rainfall Experiment (SCMREX). *Bull. Amer. Meteor. Soc.*, **98**, 999–1013, https://doi.org/10.1175/BAMS-D-15-00235.1.

McMillen, J. D., and W. J. Steenburgh, 2015: Capabilities and limitations of convection-permitting WRF simulations of lake-effect systems over the Great Salt Lake. *Wea. Forecasting*, **30**, 1711–1731, https://doi.org/10.1175/WAF-D-15-0017.1.

Mlawer, E. J., S. J. Taubman, P. D. Brown, M. J. Iacono, and S. A. Clough, 1997: Radiative transfer for inhomogeneous atmospheres: RRTM, a validated correlated-k model for the longwave. *J. Geophys. Res.*, **102**, 16 663–16 682, https://doi.org/10.1029/97JD00237.

Myers, J. L., and A. D. Well, 2003: *Research Design and Statistical Analysis*. 2nd ed. Chapman and Hall, 760 pp.

Schwartz, C. S., 2017: A comparison of methods used to populate neighborhood-based contingency tables for high-resolution forecast verification. *Wea. Forecasting*, **32**, 733–741, https://doi.org/10.1175/WAF-D-16-0187.1.

Skamarock, W., and Coauthors, 2008: A description of the Advanced Research WRF version 3. NCAR Tech. Note NCAR/TN-475+STR, 113 pp., https://doi.org/10.5065/D68S4MVH.

Sobash, R. A., J. S. Kain, D. R. Bright, A. R. Dean, M. C. Coniglio, and S. J. Weiss, 2011: Probabilistic forecast guidance for severe thunderstorms based on the identification of extreme phenomena in convection-allowing model

forecasts. *Wea. Forecasting*, **26**, 714–728, https://doi.org/10.1175/WAF-D-10-05046.1.

Squitieri, B. J., and W. A. Gallus, 2016: WRF forecasts of Great Plains nocturnal low-level jet-driven MCSs. Part I: Correlation between low-level jet forecast accuracy and MCS precipitation forecast skill. *Wea. Forecasting*, **31**, 1301–1323, https://doi.org/10.1175/WAF-D-15-0151.1.

Stensrud, D. J., 1996: Importance of low-level jets to climate: A review. *J. Climate*, **9**, 1698–1711, https://doi.org/10.1175/1520-0442(1996)009<1698:IOLLJT>2.0.CO;2.

Wang, C., F. Chien, S. Paul, D. Lee, and P. Chuang, 2017: An evaluation of WRF rainfall forecasts in Taiwan during three mei-yu seasons from 2008 to 2010. *Wea. Forecasting*, **32**, 1329–1351, https://doi.org/10.1175/WAF-D-16-0190.1.

Wang, H., Y. Luo, and B. Jou, 2014: Initiation, maintenance, and properties of convection in an extreme rainfall event during SCMREX: Observational analysis. *J. Geophys. Res. Atmos.*, **119**, 13 206–13 232, https://doi.org/10.1002/2014JD022339.

Wang, S., and A. H. Sobel, 2017: Factors controlling rain on small tropical islands: Diurnal cycle, large-scale wind speed, and topography. *J. Atmos. Sci.*, **74**, 3515–3532, https://doi.org/10.1175/JAS-D-16-0344.1.

Wilks, D. S., 1995: *Statistical Methods in the Atmospheric Sciences: An Introduction*. Academic Press, 467 pp.

Wu, M., and Y. Luo, 2016: Mesoscale observational analysis of lifting mechanism of a warm-sector convective system producing the maximal daily precipitation in China mainland during pre-summer rainy season of 2015. *J. Meteor. Res.*, **30**, 719–736, https://doi.org/10.1007/s13351-016-6089-8.

Zhang, M., and Z. Meng, 2018: Impact of synoptic-scale factors on rainfall forecast in different stages of a persistent heavy rainfall event in south China. *J. Geophys. Res. Atmos.*, **123**, 3574–3593, https://doi.org/10.1002/2017JD028155.

——, ——, Y. Huang, and D. Wang, 2019: The mechanism and predictability of an elevated convection initiation event in a weak-lifting environment in central-eastern China. *Mon. Wea. Rev.*, **147**, 1823–1841, https://doi.org/10.1175/MWR-D-18-0400.1.

Zhang, X., Y. Luo, Q. Wan, W. Ding, and J. Sun, 2016: Impact of assimilating wind profiling radar observations on convection-permitting quantitative precipitation forecasts during SCMREX. *Wea. Forecasting*, **31**, 1271–1292, https://doi.org/10.1175/WAF-D-15-0156.1.

Zhou, X., and Coauthors, 2003: *1998 Huanan Area Meso scale Experiment (HUAMEX)* (in Chinese). China Meteorological Press, 220 pp.